Data Analysis and Results of the Ka-Band Array Feed Compensation System–Deformable Flat Plate Experiment at DSS 14

P. Richter,[1] M. Franco,[2] and D. Rochblatt[2]

The natural radio-source antenna-temperature data acquired by both the array-feed compensation system (AFCS) and the deformable flat plate (DFP) system at 32 GHz (Ka-band) during the experiment conducted during the winter of 1998–1999 to compare the performance of the two systems at DSS 14 are analyzed and final results obtained in the form of aperture-efficiency-versus-elevation curves. Particular attention is given to analyzing the noise and pointing characteristics of the two systems and the impact of these characteristics on the results obtained.

Comparisons are made of the results obtained with the two systems with earlier Ka-band and 8.4-GHz (X-band) efficiency measurements at DSS 14 and with theoretical computations based on finite-element model predictions and holography measurements. Excellent agreement has been achieved with all of these approaches, with the result that the Ka-band performance of the 70-m antenna, both with and without compensation for the effects of gravity deformation, is now well understood.

The uncompensated Ka-band aperture efficiency at the mean rigging angle of 41.5 deg is 31.0 ± 1.5 percent, while the gain improvement resulting from the two systems, each acting alone, ranges from approximately 2 dB at low elevations to between 2.7 and 4.4 dB at 85 deg, the higher value corresponding to the AFCS measurements.

I. Introduction

During the period from November 1998 through February 1999, a series of measurements was carried out on the 70-m antenna at DSS 14 to determine the performance characteristics of two systems designed to compensate for the effects of elevation-dependent gravity distortion of the main reflector on antenna gain. The array feed compensation system (AFCS) and the deformable flat plate (DFP) system were

---

[1] Communications Systems and Research Section.

[2] Communications Ground Systems Section.

both mounted in the same feed cone (the holography cone), and each was used to independently measure the antenna-aperture efficiency as a function of elevation by observing natural radio sources.[3]

This article describes the analysis and reduction of the data acquired during the AFCS–DFP experiment and presents the results obtained. A companion article appearing in this issue describes the design and performance of the AFCS in detail [1], and a forthcoming article will describe the design and performance of the DFP system, including the procedures used to determine the correct actuator settings from holographic wavefront error measurements.

For each of the two systems, the analyzed data consisted of antenna temperatures for natural radio sources measured as a function of azimuth and elevation during the various observational periods, in addition to accompanying pointing and calibration data. The radio sources measured during the investigation, and used for the performance assessments for both systems, were 3C84, 3C273, and 3C274, the first two being variable point sources that must be calibrated against a standard and the latter being the DSN standard calibrator.

In the case of the AFCS, the measured quantities for the central feed and for the combined power of all seven feeds were analyzed and compared, while, for the DFP system, the measured quantities for the plate both flat and flexed were analyzed and compared.

The AFCS is self contained in that it consists of seven nominally identical receiver channels, each with its own RF front end and IF amplifier [1], while the DFP system used the Ka-band test package (TPR) to make the measurements [2].[4] The two systems were located at different positions in the optical path, the AFCS feeds being at the antenna Cassegrain focus, F1, and the TPR feed at the 1:1 reimaged focus, F2, located below F1 after reflection from an ellipsoidal mirror and the DFP (see Fig. 1).

As a consequence of differences in their characteristics, the measured data for the two systems also displayed differences, the most obvious and significant being the nature of the noise. Thus, the AFCS source temperature measurements were dominated by receiver noise, while those for the TPR were dominated by pointing errors, and this led to a somewhat different approach in the reduction of the two sets of data to the final aperture-efficiency-versus-elevation curves that provide the measure of each system's performance.

The following sections describe the system characteristics and data-analysis procedures in greater detail and present the final results of the measurements.

II. Data Acquisition

The nature of the AFCS data is best understood by referring to Fig. 2, which shows the time line for a typical measurement segment. This begins with a 50-mdeg cross-elevation offset from the source predict position to measure the background system operating temperature.[5] This is followed by a sequence of ± 4-mdeg cross-elevation offsets and a similar sequence of ± 4-mdeg elevation offsets that are used to determine the cross-elevation and elevation pointing corrections required to correct for pointing errors accumulated since the previous measurement sequence.

---

[3] Other experiments carried out with the AFCS and DFP involved continuous-wave (CW) measurements and the simultaneous use of the two systems to achieve further improvement in performance. These will be discussed in a separate article at a future date.

[4] While the term TPR has the generic meaning "total power radiometer," which in fact describes all of the radiometers used in the experiments being reported on here, it has been used to refer specifically to the Ka-band test package in the AFCS–DFP experiment, and that usage will be maintained throughout this article.

[5] The nominal half-power beam width (HPBW) of the DSS-14 antenna beam at Ka-band is 9.0 mdeg.
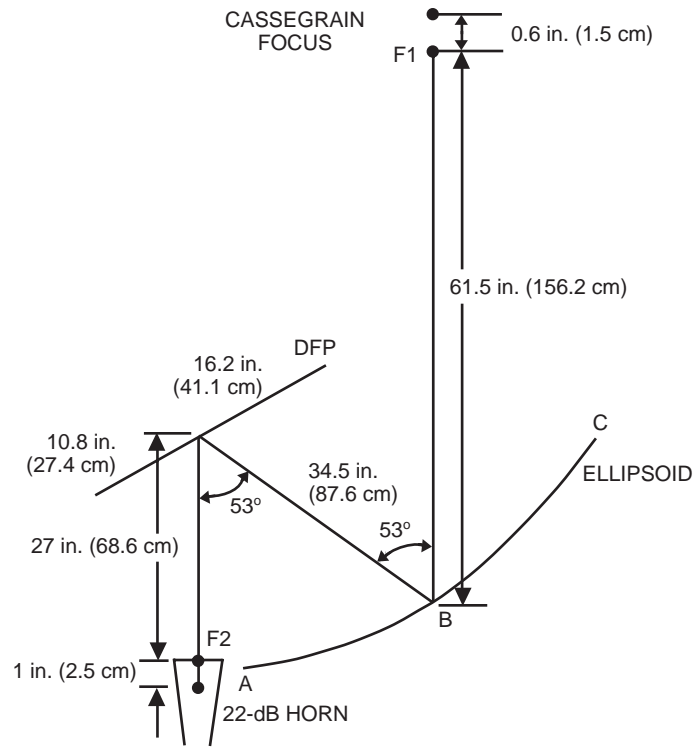
Fig. 1. The RF optics design inside the holography cone, showing the geometry that enables both separate AFCS and DFP measurements at F1 and F2, respectively, and joint AFCS–DFP measurements at F2. The antenna Cassegrain focus was 0.6 in. (1.5 cm) above F1, which was corrected for by alignment of the subreflector in the z-axis.
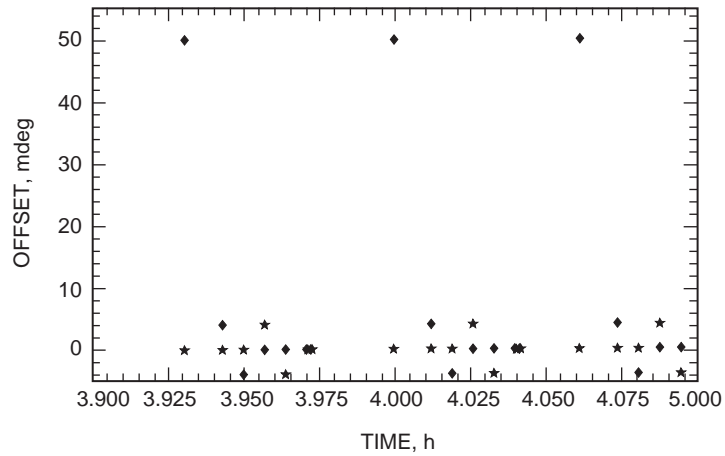

Fig. 2. The sequence of cross-elevation (diamond) and elevation (star) offsets used in determining the AFCS pointing corrections and source temperatures.

Finally, the beam is positioned to the predict value and then to the corrected predict value, using the pointing corrections just determined.[6] The source temperature is then calculated as the difference of the on-source and off-source system operating temperatures, and the process is repeated as the source is tracked.

A similar boresighting procedure was used to acquire the DFP source temperature data. Here, however, instead of starting with a single off-source measurement, the antenna beam first was moved in cross-elevation in a stepwise sequence consisting of the five offset values, -5, -0.5, 0, $+0.5$, and $+5$ HPBWs. After subtracting a linear background term from the temperature data, determined from the outermost points, a Gaussian function was fitted to the remaining three points, and a peak source temperature, HPBW, and cross-elevation pointing correction determined from the Gaussian fitting parameters.[7]

The procedure was then repeated in the elevation direction after first applying the previously determined cross-elevation pointing correction to fix the elevation scan location.[8] Similarly, the five data points were then used to determine a linear background term and a Gaussian function from which a new set of peak source temperature, HPBW, and elevation pointing-correction values was found. The entire process was then repeated as the source was tracked.

III. Noise-Level Analysis

The AFCS and the DFP measuring systems have distinctly different noise characteristics. In general, the fluctuations of the detected outputs of the radiometers are functions of the system operating temperature, T_{op}; the RF system bandwidth, B; the integration time, τ, used during the measurements; and the duration of a given measurement, t_D.

Table 1 summarizes the relevant parameters of the two measuring systems.

Table 1. System parameters affecting radiometer-output noise.

System	T_{op}, K	B, MHz	τ, s	t_D, s
AFCS	100	0.08	1	144
DFP	100	200	5	90

The above values may be used to estimate the noise level of the source temperature measurements, based on a model of the dominant processes contributing to the noise fluctuations in the detected receiver output. Previous measurements of the characteristics of the TPR output fluctuations, specifically their power spectral density (PSD) over the frequency range $6.5 \times 10^{-5} < f < 0.5$ Hz, resulted in the following expression:

$$S_{T_{op}}(f) = S_0 + \frac{K_1}{f^2} + \frac{K_2}{f^{8/3}} \quad \text{K}^2/\text{Hz}$$

---

[6] The pointing corrections are determined by fitting a quadratic function to the offset and on-source data points for each direction. In order to prevent overshoot, the actual corrections applied are only 70 percent of the calculated values, the intent being to achieve close to critical damping in the correction process.

[7] Since the system is critically determined, there being three parameters and three data points, the "fit" is exact, and the Gaussian passes through all three data points exactly.

[8] Here, the full correction is applied.

where

$$S_0 = 1.50 \times 10^{-4} \ \text{K}^2/\text{Hz}$$

$$K_1 = 1.64 \times 10^{-6} \ \text{K}^2/\text{s}$$

$$K_2 = 2.36 \times 10^{-7} \ \text{K}^2/\text{s}^{5/3}$$

and f is the frequency of the fluctuations.[9] This result may be used to derive the corresponding standard deviation of the output fluctuations:

$$\sigma_{T_{op}}\left(\tau, t_D\right) = T_{op}\sqrt{\frac{1}{B\tau} + \frac{2\pi^2 K_1}{3 \times 10^4}\, t_D + \frac{18.3 K_2}{T_{op}^2}\, t_D^{5/3}} \ \ \text{K}$$

where τ is the integration time used in the measurements and t_D is the total time duration of the measurement.[10]

The three terms appearing in the expressions for the PSD and standard deviation correspond to three distinct processes, the first being thermal noise, the second radiometer instability due to temperature drift of electronic components and flicker phenomena, and the third fluctuations in the received power due to tropospheric density fluctuations.

The coefficients appearing in the above expression for the PSD are specific to the Ka-band test package and were obtained with the feed pointing at the zenith sky. The similar design of the AFCS radiometers implies that similar values apply to this system as well, so that we may obtain an approximate comparison of the two systems by assuming the same coefficients for each one.

Applying the above expression for the standard deviation of the random fluctuations to the two sets of radiometer data given in Table 1, we then find the following predicted values for the zenith:

$$\text{AFCS}: \ \sigma_{T_{op}} = 0.379 \ \text{K}$$

$$\text{DFP}: \ \sigma_{T_{op}} = 0.094 \ \text{K}$$

The four-to-one difference seen here results from a distinctly different mix of the three contributions to the noise fluctuations, as can be seen from the comparison of the corresponding variances for these terms in Table 2.

Table 2. Computed variances for the individual terms contributing to the total radiometer-output variance.

System	Thermal noise, K^2	Gain fluctuations, K^2	Tropospheric fluctuations, K^2
AFCS	0.125	0.00155	0.0170
DFP	1.0×10^{-5}	9.7×10^{-4}	7.8×10^{-3}

[9] P. Richter, Communications Systems and Research Section, Jet Propulsion Laboratory, Pasadena, California, unpublished results.

[10] Ibid.

Thus, the AFCS, by virtue of its narrow bandwidth, is dominated by thermal noise, while the TPR system used to characterize the DFP is dominated by tropospheric fluctuations. This implies that the AFCS noise background is elevation independent, whereas the DFP system noise background will depend on the elevation since the coefficient K_2 is elevation dependent.

In order to apply these calculated $\sigma_{T_{op}}$ values to the source temperature measurements, one must take into account the algorithm used to compute the latter. For the AFCS, this is a simple subtraction of the off-source and on-source T_{op} values so that the noise level of the source temperature measurements is just $\sqrt{2} \times \sigma_{T_{op}} = 0.536$ K.

For the DFP, on the other hand, the situation is more complex. The AUTOBORE algorithm used by the TPR computes the peak source temperature in two steps [3]. First, the off-source level is determined from a straight line fit to the two off-source measurements at ± 5 HPBWs, and the variance of the uncertainty in this measurement is $\sigma_{off}^2 = \sigma_{T_{op}}^2/2$. The difference between the on-source and off-source levels then is found by subtracting this off-source value from the remaining three points and fitting the results to a Gaussian approximation to the beam pattern. The subtraction leads to an effective variance of the three data points of $\sigma^2 = \sigma_{T_{op}}^2 + \sigma_{off}^2 = 1.5\sigma_{T_{op}}^2$, and the variance of the peak source temperature determined from the Gaussian fit is given by $\sigma_{T_{pk}}^2 = \sigma^2 = 1.5\sigma_{T_{op}}^2$ [4]. Thus, the estimated standard deviation of the DFP source temperature measurements is $\sigma_{T_{pk}} = \sqrt{1.5} \times \sigma_{T_{op}} = 0.12 \ K$.

Actual measurements of the standard deviations of the noise fluctuations present in the source temperature measurements made with each system yield the following typical values:

$$\text{AFCS}: \sigma_{T_{pk}}(3\text{C}84) = 0.45 \text{ K}$$
$$\sigma_{T_{pk}}(3\text{C}273) = 0.62 \text{ K}$$
$$\text{DFP}: \sigma_{T_{pk}}(3\text{C}84) = 0.07 \text{ K}$$
$$\sigma_{T_{pk}}(3\text{C}273) = 0.11 \text{ K}$$

Considering that these measurements include all elevation angles, and that the value of K_2 can vary significantly from day to day, the agreement with the model calculations presented above is remarkably good.

IV. Pointing Errors

The AFCS and DFP data sets both show evidence of periods of good pointing and periods of bad pointing that can be distinguished from one another by analyzing the pointing error and/or the pointing-correction records. The two extremes can be separated by removing those points lying outside the $\pm 3\sigma$ range from the complete data sets, for example, and when this is done, the good pointing data for both systems show good internal consistency.

An example of good AFCS pointing data is shown in Fig. 3, where the cross-elevation and elevation pointing corrections are plotted against time over a period of 1.1 h. Also shown are polynomial fits to the data, it being assumed that these slowly varying functions provide a good estimate of the true corrections that would actually point the beam directly on the source. The residuals to these fits thus estimate the actual pointing errors, and when these are combined to produce the residual radial errors, the result shown in Fig. 4 is obtained. These residual radial pointing errors have a mean value over the interval shown of 0.145 mdeg, corresponding to a mean pointing loss of 0.07 percent, so that, by considering only those data corresponding to good pointing, the errors in determining peak source temperatures are effectively unbiased and dominated by the radiometer thermal noise, as discussed in the previous section.
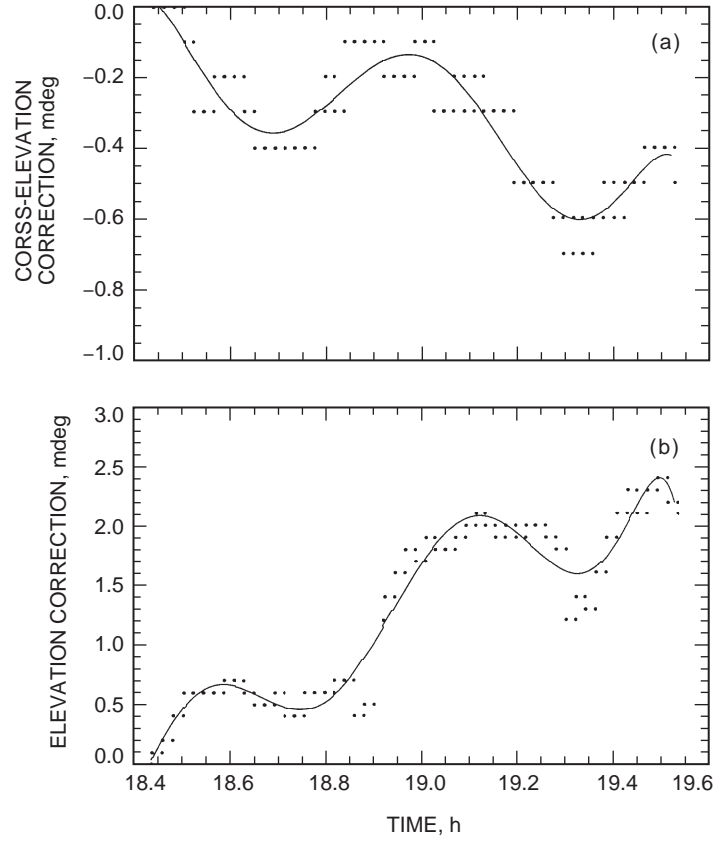
Fig. 3. Typical good AFCS pointing-correction data with polynomial fits from which the residual errors may be determined: (a) cross-elevation correction and (b) elevation correction versus UTC for 3C273 on DOY 360. The digital resolution of 0.1 mdeg sets a limit on the accuracy with which the residuals can be determined.
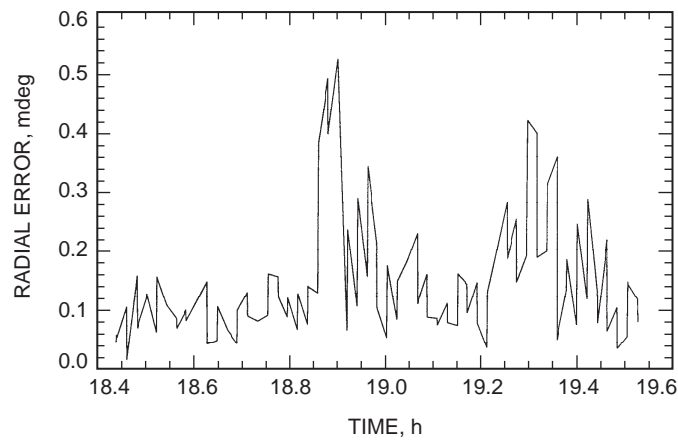

Fig. 4. The radial errors computed from the residuals shown in Fig. 3. The mean value for the interval shown is 0.145 mdeg.

7

The situation for the DFP radial pointing errors is illustrated in Fig. 5, where it is seen that these are several times those found for the AFCS. The mean radial error for the segment of good data shown in the figure is 0.718 mdeg, and the mean value found for all of the DFP data is 0.726 mdeg, corresponding to a mean pointing loss of 1.79 percent. Also manifest from Fig. 5 is an apparent toggling back and forth between high and low errors, which, recalling that this system applies the full cross-elevation and elevation corrections for each measurement, is possibly the result of overcorrection.[11]

The relatively large pointing errors shown in Fig. 5 imply that the source temperature data for the DFP experiment are dominated by these, and this is apparent from the efficiency plots discussed in Section VI, which show substantial downward bias coupled with a sharply defined maximum value at each elevation.
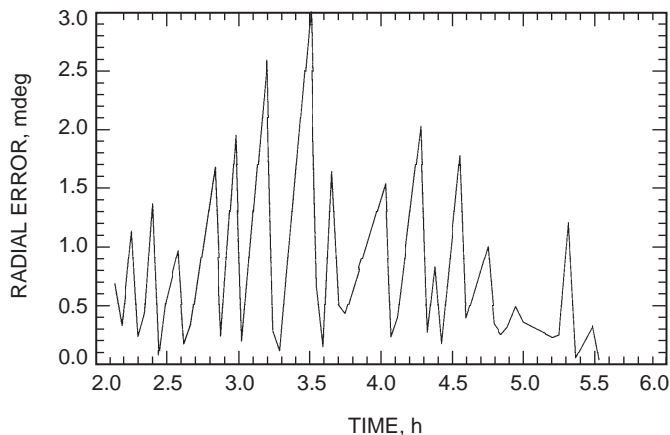
Fig. 5. The radial errors computed for a typical segment of DFP data. The mean value for the interval shown is 0.718 mdeg, while that for all of the good DFP data is 0.726 mdeg.

V. Source Temperature Data

The detected power outputs for both the AFCS and DFP systems were converted to antenna system-operating temperature values by comparison with the output corresponding to the radiometer looking at an ambient load of known physical temperature. The calibration procedure also checks for system linearity by injecting noise from a noise diode while the radiometer is looking at the sky and at the ambient load [5].

The source temperature values computed from these, T_{pk}, were subsequently corrected for atmospheric absorption and calibrated against the standard source 3C274, whose flux density and source size correction for the 70-m antennas at Ka-band are considered well-known.[12]

The atmospheric absorption corrections were determined from measured tipping-curve data acquired at approximately the same time the radio source measurements were made. These data are of the form

---

[11] The AFCS and DFP measurements were carried out during the same period of time during clear, dry weather with little or no wind, and each utilized a similar boresight algorithm to determine the pointing errors and correct for them. The only obvious difference between the two systems appears to be that the AFCS applied only 70 percent of the measured pointing error as a correction, while the TPR system applied the whole measured error as a correction.

[12] P. Richter, *Radio Source List for Antenna Calibration*, DSN 890-269, JPL D-3801 (internal document), Jet Propulsion Laboratory, Pasadena, California, October 15, 1994.

$$T_{op}\,(el) = T_r + T_c' e^{-\tau/\sin(el)} + T_A\left(1 - e^{-\tau/\sin(el)}\right)$$

$$\cong T_r + T_c' + (T_A - T_c')\,\tau\,\csc\,(el)$$

where T_r is the receiver noise temperature, including the follow-on amplifier; T_c' is the effective cosmic background temperature[13] (=2.0 K); T_A is the effective radiating temperature of the atmosphere (=270 K for clear, dry weather); and τ is the optical depth of the atmosphere.

Thus, a plot of T_{op} versus $\csc\,(el)$, coupled with a knowledge of T_A and T_c', yields the value for τ, and this was applied to the measured T_{pk} values to determine their vacuum values, i.e., $T_{pk_0}\,(el) = T_{pk}\,(el)\,e^{\tau/\sin(el)}$, where the subscript zero refers to the vacuum value and the unsubscripted term is the measured value.

In order to calibrate the variable point source data against the standard source 3C274, one must have T_{pk} versus el data for each source over a common range of elevation so that the ratio of the two can be found. Then, the flux density of the variable source is given by

$$S = \frac{T}{T_0}\frac{S_0}{C_{r_0}}$$

where the subscript zero here corresponds to the calibrator, 3C274, and C_{r_0} is the source size correction factor for this source.

Using the values for 3C274 for the 70-m antennas at Ka-band, $S_0 = 16.22$ Jy, $C_{r_0} = 1.90$, and the experimentally measured ratios,

$$\frac{T(3C84)}{T_0} = 1.57$$

$$\frac{T(3C273)}{T_0} = 4.58$$

the Ka-band flux densities for these sources were found to be[14]

$$S(3C84) = 8.54 \text{ Jy}$$

$$S(3C273) = 13.10 \text{ Jy}$$

The source temperature value for a 100 percent aperture-efficiency antenna is given by

$$T_A = \frac{AS}{2kC_r}$$

where A is the aperture area and k is Boltzmann's constant. Substituting the above flux density values, we find[15]

---

[13] This includes a correction to the actual temperature to account for the difference between the Planck and Rayleigh–Jeans black body radiation laws at 32 GHz.

[14] Since there was relatively little overlap of elevation in the AFCS data, and these data were noisier than the DFP data, these ratios were determined from the DFP data only. The close time proximity of the AFCS and DFP efficiency measurements guarantees the constancy of the flux densities of these two sources during the measurement period.

[15] The values calculated here are for the time period during which the measurements were made, namely from the latter part of December 1998 through early February 1999.

$$T_A(3C84) = 18.68 \text{ K}$$

$$T_A(3C273) = 54.49 \text{ K}$$

and these values were used to calculate the aperture efficiencies as a function of elevation for the various parts of the experiment, using the expression

$$\varepsilon(el) = \frac{T_{pk_0}(el)}{T_A}$$

VI. Fitting to the Aperture Efficiency Data

A. The Baseline Measurements

The general appearance of the aperture-efficiency-versus-elevation data suggests that the conventional approach to fitting with a low-order polynomial is not appropriate here. In fact, as is shown below, three independent lines of evidence yield very similar looking efficiency curves for the current baseline performance (no gravity compensation) of the DSS-14 antenna at Ka-band:

(1) Predictions based on transforming the 1988 X-band efficiency results obtained immediately after the 70-m upgrade to Ka-band, using the Ruze–Levy equation

(2) Predictions based on finite-element model calculations of the main-reflector distortion due to gravity, also using the Ruze–Levy equation

(3) Ka-band efficiency measurements made with the AFCS central feed and with the DFP unflexed

1. The AFCS Data. Figure 6 shows the 3C84 and 3C273 AFCS central-channel-efficiency-versus-elevation data, corrected for atmospheric absorption and calibrated against 3C274, together with a fitting curve based on the Ruze–Levy equation. The Ruze–Levy equation gives the aperture efficiency as a function of elevation by expressing the rms half-path-length deviation of the wavefront error, $\Sigma(el)$, in terms of computed parameters based on the structural analysis of the main reflector, subject to gravitational distortion [6]. Thus, the aperture efficiency is given by

$$\varepsilon(el) = \varepsilon_m \exp\left[-\left(\frac{4\pi\Sigma(el)}{\lambda}\right)^2\right]$$

where

$$\Sigma^2 = S_y^2\eta^2 + S_z^2\zeta^2 + 2CS_yS_z\eta\zeta$$

$$S_y = \text{rms half-path-length deviation for the y-axis load } (el = 0 \text{ deg})$$

$$S_z = \text{rms half-path-length deviation for the z-axis load } (el = 90 \text{ deg})$$

$$\eta = \cos el_m - \cos el$$

$$\zeta = \sin el_m - \sin el$$

$$C = \text{correlation coefficient between the y-axis and z-axis load deviations}$$

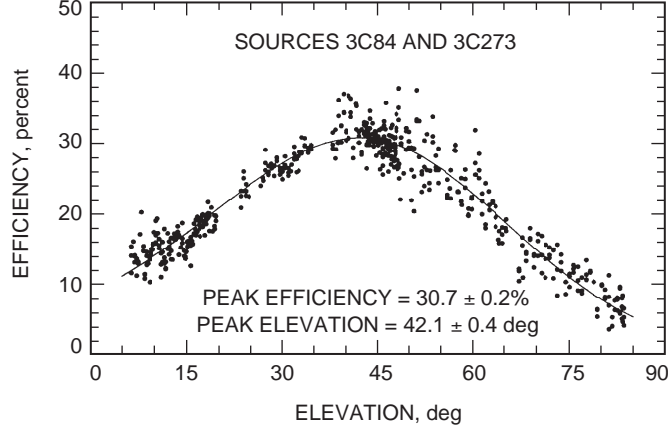$$\varepsilon_m = \text{maximum aperture efficiency (at } el = el_m)$$

Fig. 6. Aperture efficiency versus elevation measured by the AFCS central channel. The data have been corrected for atmospheric absorption and calibrated against the source 3C274.

The peak efficiency, ε_m, may be expressed in terms of the elevation-independent rms half-path-length deviation, Σ_0, due to panel-setting errors, subreflector irregularities, etc., and other losses, ε_a, that result from truncation and attenuation of the wavefront amplitude, such as spillover, blockage, and ohmic losses, i.e., $\varepsilon_m = \varepsilon_a \exp[-(4\pi\Sigma_0/\lambda)^2]$.

The nonlinear, least-squares fitting to the Ruze–Levy equation involves the five parameters ε_m, S_y, S_z, C, and el_m. However, within the limits of the range $-1 < C < 0$, the χ^2 value for the fit is almost independent of C, and consequently this parameter was set equal to zero, as predicted by the finite-element model calculations.[16] By so doing, the values of S_y and S_z determined from the fit can be compared with those calculated from the finite-element model.[17]

The results of fitting to the data shown in Fig. 6, with C set equal to zero, are

$$\varepsilon_m = 30.68 \pm 0.17 \text{ percent}$$
$$S_y = 1.42 \pm 0.04 \text{ mm}$$
$$S_z = 1.13 \pm 0.04 \text{ mm}$$
$$el_m = 42.06 \pm 0.36 \text{ deg}$$

while the values calculated from the finite-element model are $S_y = 1.674$ mm and $S_z = 0.800$ mm.[18]

It is also worth noting that the data shown in Fig. 6 are normally distributed about the mean defined by the fit, as can be seen from Fig. 7, which shows the frequency distribution of the fit residuals. This provides further support for the conclusions reached in Section III regarding the nature of the AFCS measurement noise, namely, that it is dominated by thermal fluctuations.

The X-band aperture-efficiency data acquired at DSS 14 in 1988, following the 70-m upgrade, were also fitted by the Ruze–Levy equation. The parameter values that resulted in the best fit to the 434 data points spread over the elevation range from 10 through 85 deg were [7]

---

[16] For values of $C \to +1$, the efficiency curve becomes very flat over the entire elevation range.

[17] The parameters S_y and S_z are not directly measurable, but rather correspond to the rms values induced when gravity is "turned on" with the antenna pointing, respectively, at the horizon and the zenith.

[18] D. Strain, personal communication, Planning Research Corporation, Pasadena, California, with the Communications Ground Systems Section, Jet Propulsion Laboratory, Pasadena, California, 1999.
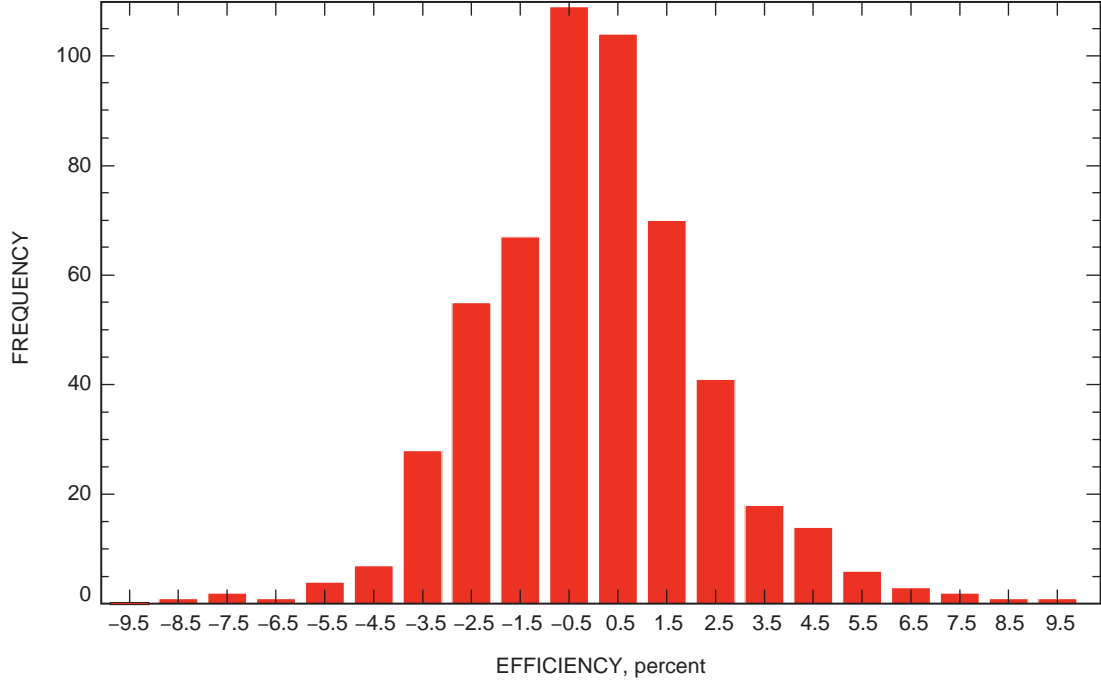
Fig. 7. Frequency distribution of the residuals to the fit shown in Fig. 6, demonstrating their normal distribution about the mean and, thus, validating the assumption that the noise in these measurements is dominated by thermal effects and not pointing errors.

$$S_y = 1.173 \text{ mm}$$

$$S_z = 0.531 \text{ mm}$$

$$C = -0.9935$$

$$el_m = 45.93 \text{ deg}$$

Here, the correlation, C, was included as a fitting parameter. This means that the obtained values of S_y and S_z cannot be directly compared with those found above, since the large negative value of C has been offset by correspondingly different S_y and S_z values that result in virtually the same χ^2 value and curve shape as would be found with $C = 0$.

However, one *can* directly compare the Ka-band efficiency curve given by these parameters with that obtained above by substituting the Ka-band wavelength of 9.37 mm for the X-band value of 35.60 mm in the Ruze–Levy equation and adjusting the two curves to coincide at the peak. Thus, setting $\varepsilon_m = 30.68$ percent and $el_m = 42.06$ deg, and using the X-band values for C, S_y, and S_z, we obtain the curve shown in Fig. 8, which also shows the AFCS central-channel efficiency curve and that predicted by the finite-element model (FEM), where the same values for ε_m and el_m have also been used in all three cases.

The general agreement between the three curves is very good, but there are clearly some differences, possibly due to subreflector distortion resulting from the Landers earthquake damage and/or misalignment of the subreflector, neither of which are accounted for in the X-band data or the finite-element model calculations.

The quality of the Ruze–Levy fit to the AFCS central-channel efficiency data can be assessed by computing the standard error for the fit as a function of elevation [4]. The resulting error curve is shown in Fig. 9, and it can be seen that the Ruze–Levy fit to the data is accurate to within ± 0.4 efficiency percent
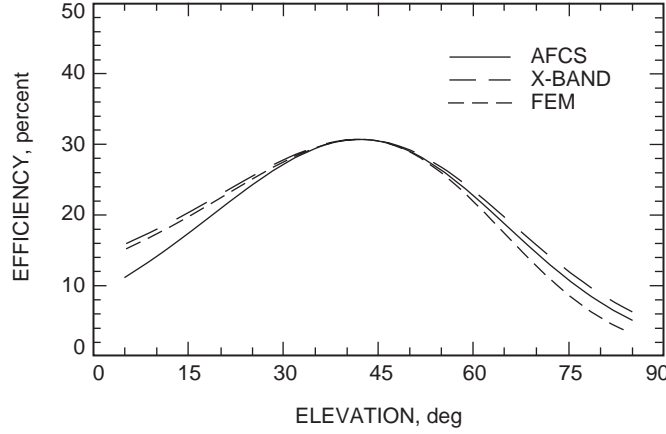
Fig. 8. Comparison of the aperture-efficiency curves for the Ruze–Levy fits to the AFCS central-channel data, the 1988 X-band DSS-14 results transformed to Ka-band, and the predictions of the finite-element model. The curves have been aligned at the peak to facilitate comparison.
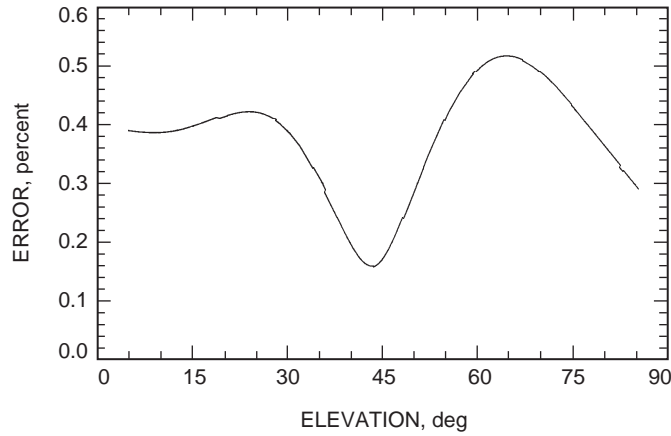

Fig. 9. The error curve of the Ruze–Levy fit to the AFCS central-feed data.

throughout most of the range, with a minimum error of ± 0.17 efficiency percent near the peak-efficiency elevation of 42.1 deg. This accuracy of the fit is consistent with the mean difference of about 0.2 efficiency percent between the fitting functions observed with $C = -1$ and $C = 0$.

As a final observation, we show the rms half-path-length deviation resulting from the Ruze–Levy fit to the AFCS central-channel data in Fig. 10. Note that this shows only the elevation-dependent component of the wavefront distortion due to gravity effects, which are presumed to vanish at the rigging angle of 42.1 deg. In actual fact, there is significant elevation-independent distortion due to panel-setting errors, subreflector distortion, and misalignments in the optical path, all represented by the term Σ_0 introduced above. In addition, there also may be some elevation-dependent effects arising from inaccuracies in the y- and z-axis focusing corrections applied to the subreflector.
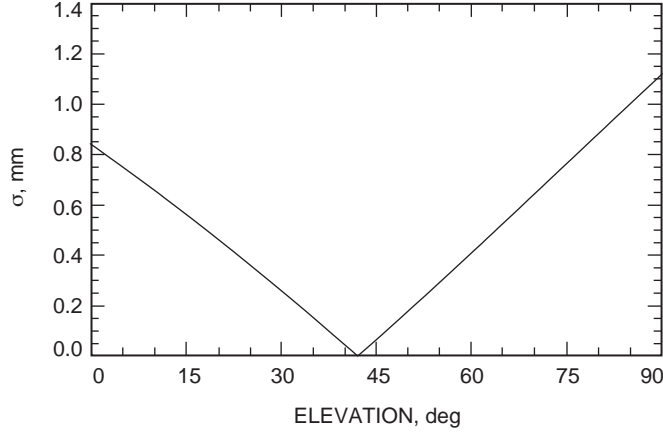
Fig. 10. The rms half-path-length deviation versus elevation for the Ruze–Levy fit to the AFCS central-channel data with the correlation $C = 0$.

2. The DFP Data. The analysis given above for the AFCS central-feed data carries through much the same for the DFP data obtained with the plate unflexed, with the following important differences:

(1) As noted in Sections III and IV, the DFP measurements are dominated by pointing errors, and the noise fluctuations are dominated by tropospheric turbulence, the result being that one cannot simply do a Ruze–Levy fit to the data as it exists.

(2) The DFP system was located at a different focal point, F2, from the AFCS during the measurements, so that additional losses were present, and these must be estimated and taken into account before attempting to compare the performance of the two systems.

As a consequence of (1) above, it was necessary to select only those data corresponding to the very best pointing before attempting a fit. This was facilitated by the relatively low residual noise due to the troposphere, so that pointing effects could be separated from tropospheric effects. Further, as a consequence of (2) above, we present both the aperture-efficiency results obtained at F2 and an estimate of those that would have been obtained at the Cassegrain focus, F1, had the DFP system been located there.

Figure 11 shows all of the efficiency data obtained with the DFP flat, and one can see from this that there is a clear upper limit to the data defined by the best pointing, and that most of the data fall below this. Ideally, one would like to be able to look at the pointing error for each point and simply remove those points for which this exceeds a value resulting in a negligible loss. Unfortunately, however, there is no obvious one-to-one correlation between the measured errors and the actual pointing error—only a statistical one—so that this approach fails.

Given the noise analysis presented in Section III, however, plus the appearance of the data shown in Fig. 11, it is possible to select the unbiased data by removing those points that statistically fall below a value predicted by the tropospheric noise level of 0.12 K (see the discussion in Section III). This condition turns out to be satisfied by means of a simple algorithm that proceeds from low elevation to the peak, near 42 deg, selecting only those points for which the efficiency always increases along the way, and repeating the same procedure in reverse, from high elevation to the peak.
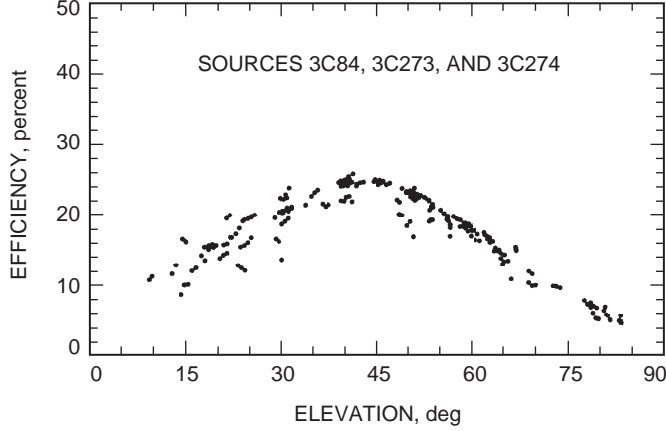
14

Fig. 11. The aperture-efficiency data acquired at F2 with the DFP unflexed, corrected for atmospheric absorption and calibrated against the source 3C274.

The results of this on the data shown in Fig. 11 are shown in Fig. 12, together with a fit by the Ruze–Levy equation with $C = 0$. The parameter values for the fit are

$$\varepsilon_m = 24.94 \pm 0.18 \text{ percent}$$
$$S_y = 1.32 \pm 0.04 \text{ mm}$$
$$S_z = 1.19 \pm 0.05 \text{ mm}$$
$$el_m = 40.94 \pm 0.37 \text{ deg}$$

and the standard deviation of the fit residuals is 0.74 efficiency percent. When this is used to compute the corresponding standard deviations of the source temperatures, one finds

$$\sigma_{T_{pk}} (3C84) = 0.14 \text{ K}$$
$$\sigma_{T_{pk}} (3C273) = 0.40 \text{ K}$$
$$\sigma_{T_{pk}} (3C274) = 0.09 \text{ K}$$

These values are approximately equal to or greater than the computed value of 0.12 K and the values of 0.07 K and 0.11 K measured for the two point sources, indicating that the procedure used to remove the biased data has effectively done so without encroaching on the unbiased data. Moreover, the shape of the fit to the unbiased data, as well as the parameter values found, are in good agreement with the results obtained with the AFCS data.

Figure 13 shows the rms error of the fit to the unbiased, unflexed DFP data as a function of elevation, and the result is seen to be similar to that found for the AFCS central-feed fit shown in Fig. 9. There is, however, a larger error at low elevations owing to the sparsity of reliable data in this range and their somewhat larger scatter. The comparison of these two figures is also interesting because it graphically illustrates how a large scatter and large number of data points (AFCS data) lead to results very similar to those obtained with a small scatter and small number of data points (DFP data).

The rms half-path-length deviation resulting from the Ruze–Levy fit to the unflexed DFP data is shown as a function of elevation in Fig. 14. Again, this shows only the elevation-dependent component of the wavefront distortion due to gravity effects.
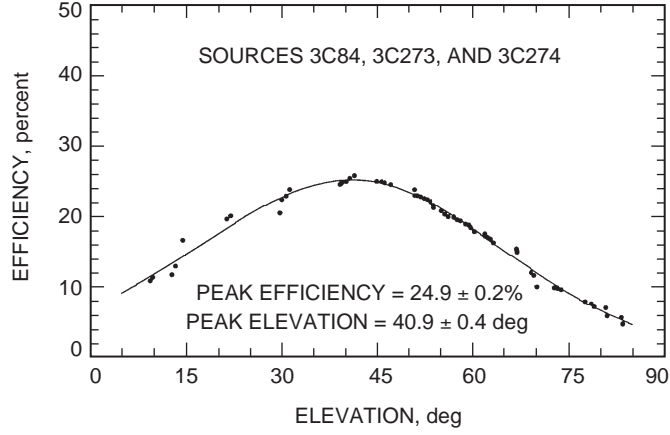
15

Fig. 12. The unbiased aperture-efficiency data at F2 with the DFP unflexed, corrected for atmospheric absorption, showing the Ruze–Levy fit to the data.
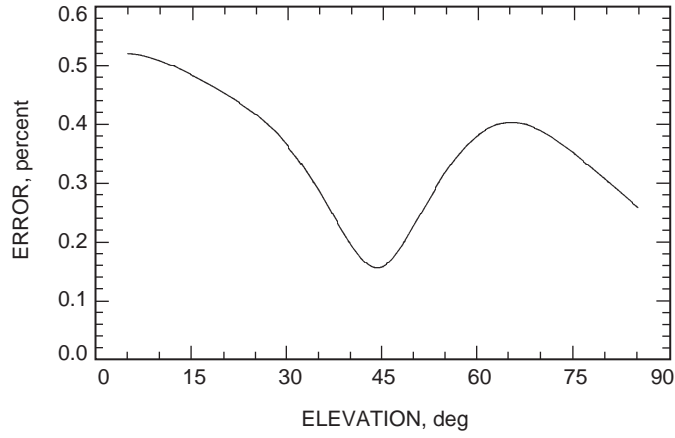

Fig. 13. The error curve of the Ruze–Levy fit to the unflexed DFP data.
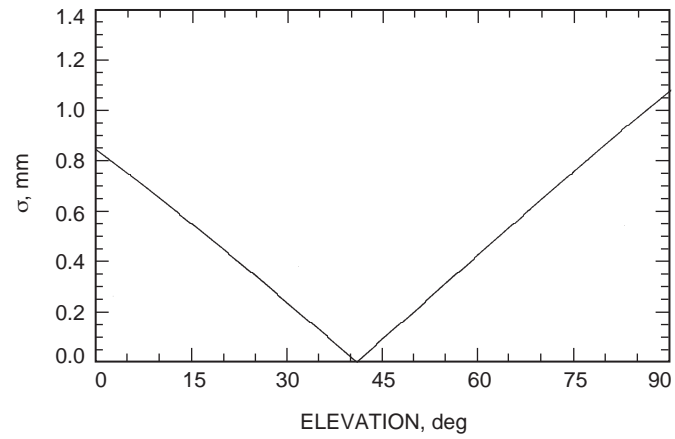

Fig. 14. The rms half-path-length deviation versus elevation for the Ruze–Levy fit to the unflexed DFP data with the correlation *C* = 0.

In order to compare the unflexed DFP efficiency results, which are based on data acquired at the focus F2, with those obtained with the AFCS central channel located at F1, two corrections were applied to the former. The AFCS measurements were referenced to the feed aperture at F1, while the DFP measurements were referenced to the radiometer flange at F2. The correction from the F2 radiometer flange to the F1 radiometer flange accounts for losses due to the ellipsoidal mirror (see Fig. 1), which are estimated to be 0.70 dB. The remaining correction is for the waveguide loss between the F1 flange and the F1 feed aperture, and this is estimated to be 0.273 dB, the total correction thus being 0.973 dB (=1.2511).

Figure 15 shows a comparison of the AFCS central-channel and unflexed DFP aperture efficiencies referenced to F1, where it is seen that the two systems produce very similar results, both in magnitude and in the shape of the efficiency-versus-elevation curve.
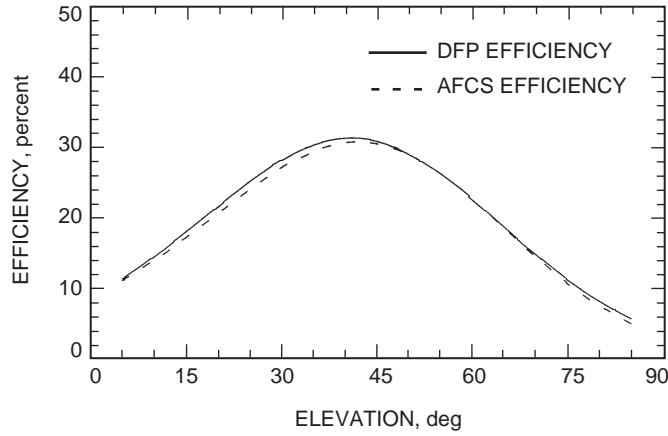
Fig. 15. Comparison of the AFCS central-channel and unflexed DFP F1 aperture-efficiency results, establishing the Ka-band baseline performance of the DSS-14 70-m antenna.

B. The Gravity-Loss Compensation Measurements

Since the analysis of the data acquired with the power of all seven AFCS feeds combined, and with the DFP flexed, carries through the same as described above for the baseline measurements for the two systems, we confine ourselves here to stating the results of the measurements and making comparisons between them.

1. The AFCS Data. Figure 16 shows the combined-power-aperture-efficiency-versus-elevation data together with the Ruze–Levy fit, again obtained by setting the correlation, C, equal to zero. The parameters obtained with the fit are

$$\varepsilon_m = 37.17 \pm 0.18 \text{ percent}$$
$$S_y = 0.90 \pm 0.03 \text{ mm}$$
$$S_z = 1.12 \pm 0.03 \text{ mm}$$
$$el_m = 39.51 \pm 0.38 \text{ deg}$$

The error curve for the fit is shown in Fig. 17 and the rms half-path-length deviation as a function of elevation in Fig. 18. Regarding the latter, it should be pointed out that this function remains a valid description of the effective wavefront error even though no *physical* compensation has taken place, as would be the case for the DFP in the flexed state.
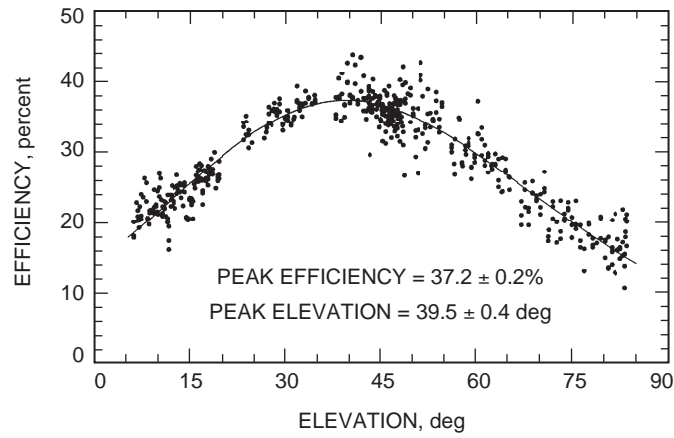
17

Fig. 16. Aperture-efficiency versus elevation for the AFCS combined power. The data have been corrected for atmospheric absorption and calibrated against the source 3C274.
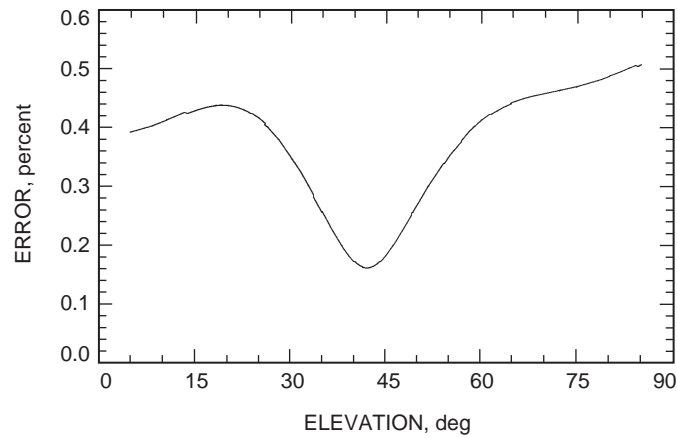

Fig. 17. The error curve of the Ruze–Levy fit to the AFCS combined power data.
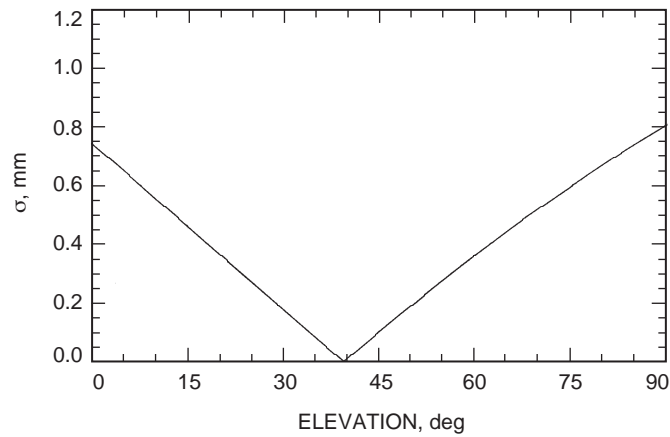

Fig. 18.   The rms half-path-length deviation versus elevation for the Ruze–Levy fit to the AFCS combined power data with the correlation _C_ = 0.

This follows as a result of the general validity of the Ruze–Levy equation, where, for the case of a wavefront error of non-gravitational origin, the function $\Sigma\,(el)$ that results in the best fit of the Ruze–Levy equation to the efficiency data accurately describes the rms half-path-length deviation, even though this results from a different cause.

Figure 19 compares the central-channel and combined-power efficiencies, showing improvement at all elevations, including the rigging angle. This implies that the wavefront error at the rigging angle, which by definition is free of gravitationally induced distortion, nonetheless contains, in addition to the high-order terms due to residual panel-setting errors, some low-order components that result in some energy in the focal plane within the outer ring of feeds. This most likely originates from some subreflector misalignment and damage to the subreflector surface sustained during the Landers earthquake.

The gain improvement resulting from power combining is shown in Fig. 20, while Fig. 21 compares the rms half-path-length deviation as a function of elevation for the central-channel and combined-channel data.
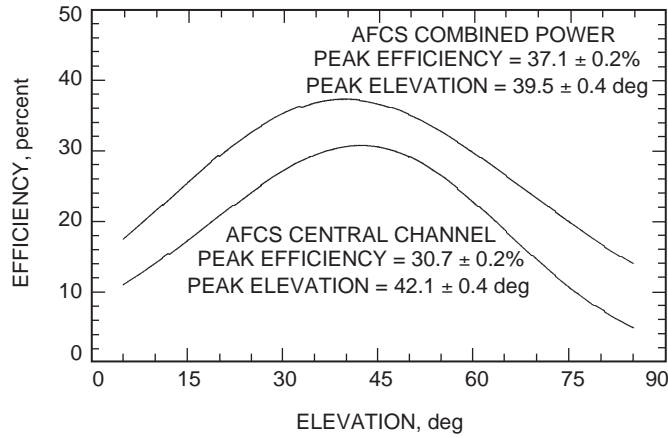
Fig. 19. Comparison of the efficiencies for the AFCS
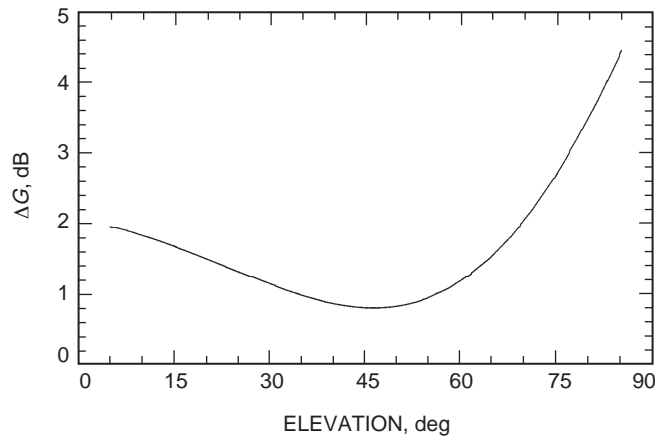central-feed and combined-power measurements.

Fig. 20. AFCS gain improvement achieved by
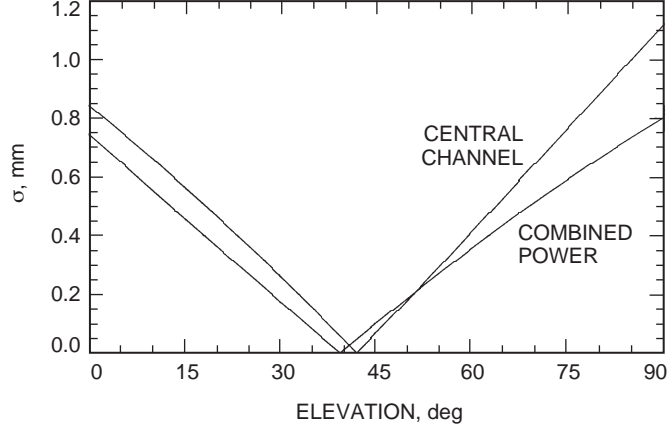combining power.

Fig. 21. Comparison of the rms half-wavelength deviations obtained with the AFCS central channel and combined power.

2. The DFP Data. The complete F2 aperture-efficiency data set resulting from flexing the DFP at selected elevations separated by 5 deg is shown in Fig. 22. Similarly to the unflexed data, we also see here a clear upper limit to the efficiency achieved at each elevation, only now the biased data result from a combination of pointing errors and non-optimal plate deformation. Nonetheless, the same rationale for selecting the unbiased data applies to the flexed data as well, and the same algorithm that was previously used may also be applied here, with the result shown in Fig. 23, which includes the Ruze–Levy fit to the data:

$$\varepsilon_m = 25.64 \pm 0.11 \text{ percent}$$
$$S_y = 1.09 \pm 0.02 \text{ mm}$$
$$S_z = 0.84 \pm 0.03 \text{ mm}$$
$$el_m = 40.83 \pm 0.29 \text{ deg}$$

Figure 24 shows the standard error curve for the fit, while Fig. 25 shows the rms half-path-length deviation as a function of elevation corresponding to the flexed data.

In Fig. 26, we compare the aperture efficiencies for the unflexed and flexed DFP, referenced to F1 (see Section VI.A.2 for details of the corrections applied in going from the F2-referenced measurements to the F1-referenced measurements), and, in Fig. 27, we show the gain improvement achieved with the DFP system. Finally, Fig. 28 compares the rms half-path-length deviations for the unflexed and flexed DFP.

VII. Comparisons Between the AFCS, DFP, and Holography Results

Figures 29 and 30 compare the results obtained with the AFCS and DFP system, showing the compensation achieved with each and indicating a somewhat greater improvement for the AFCS over most elevations. Figure 31 compares the baseline rms half-path-length deviation determined by each system, and here we see almost identical results, providing further evidence for the internal consistency of the measurements made with the two systems, as well as confidence in the overall analysis.

In addition to the AFCS and DFP aperture-efficiency measurements, holographic measurements were also carried out as part of the overall experimental methodology [8].[19] Thus, in order to determine the

---

[19] This aspect of the AFCS–DFP experiment will be the subject of a more detailed article at a future date.
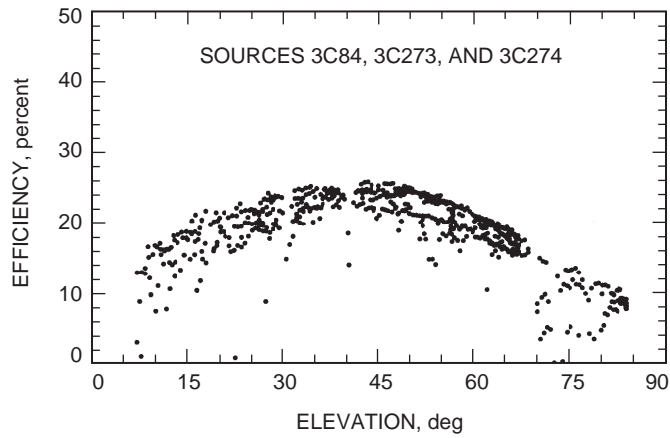
Fig. 22. The complete set of efficiency data acquired at F2 with the DFP flexed, corrected for atmospheric absorption, showing a range of compensation achieved at each elevation with different vectors determining the actuator displacements.
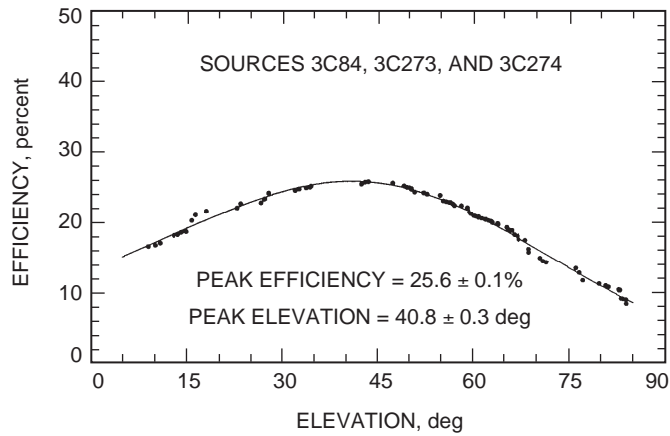

PEAK EFFICIENCY = 25.6 ± 0.1%

PEAK ELEVATION = 40.8 ± 0.3 deg

Fig. 23. The unbiased aperture efficiency data at F2 with the DFP flexed, corrected for atmospheric absorption, showing the Ruze−Levy fit to the data.
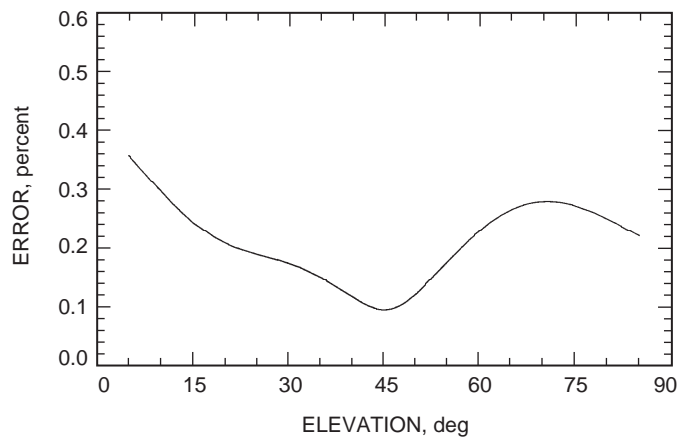

Fig. 24. The error curve of the Ruze−Levy fit to the flexed DFP data.
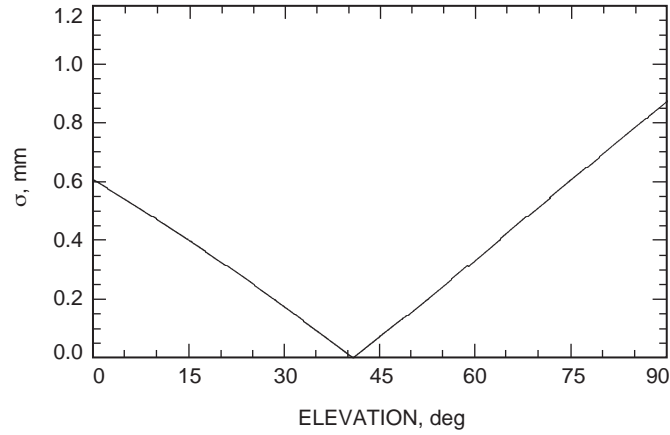
Fig. 25. The rms half-path-length deviation versus elevation for the Ruze–Levy fit to the flexed DFP data with the correlation *C* = 0.
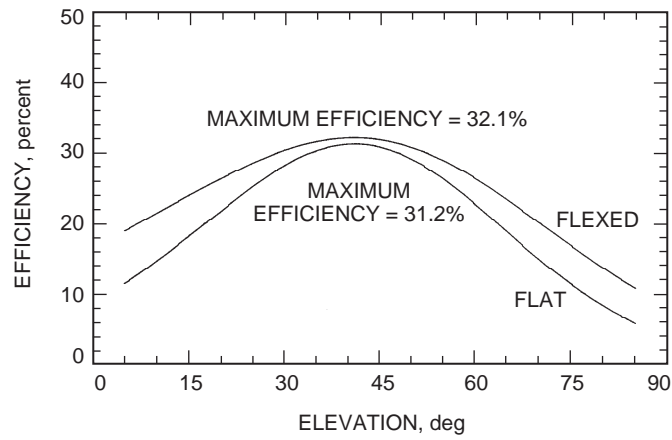

Fig. 26. Comparison of the aperture efficiency versus elevation with the DFP unflexed and flexed. In both cases, the results have been referenced to the feed aperture at the Cassegrain focus, F1.
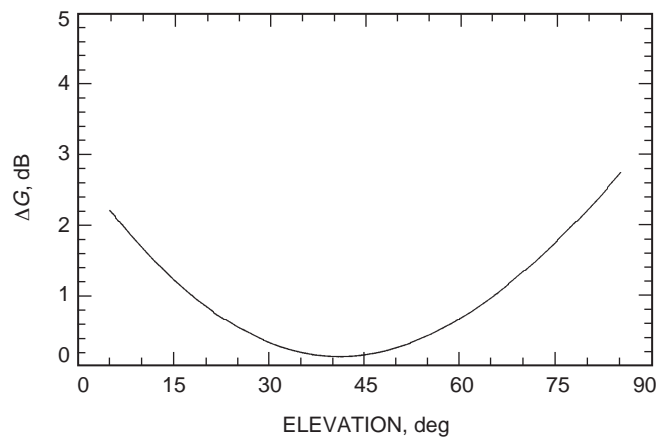

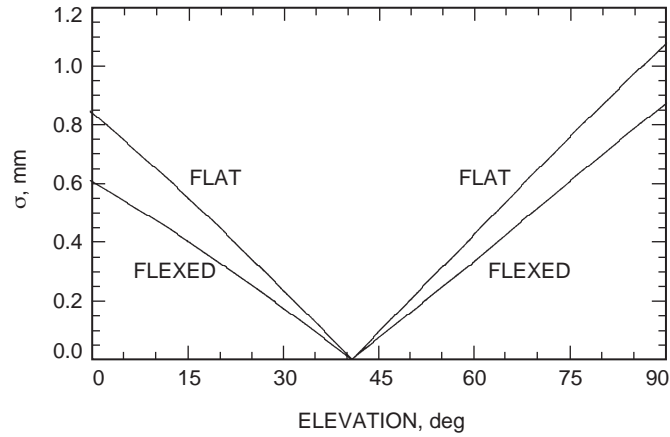**Fig. 27. Gain improvement as a function of elevation resulting from flexing the DFP.**

22

**Fig. 28. Comparison of the rms half-path-length devia-
tion versus elevation with the DFP flat and flexed.**
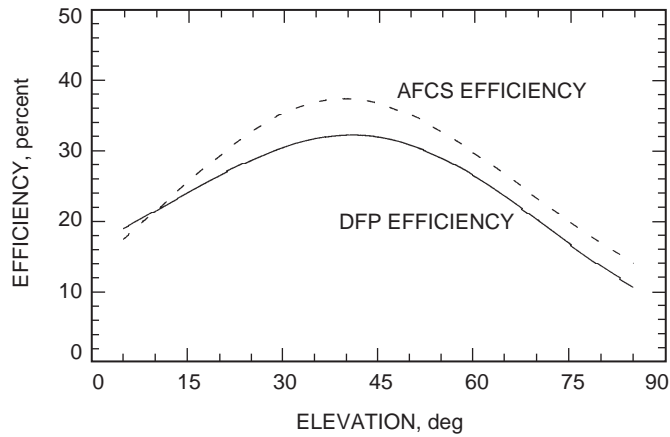

**Fig. 29.   Comparison of the AFCS and DFP aperture effi-
ciencies with both systems providing compensation.**
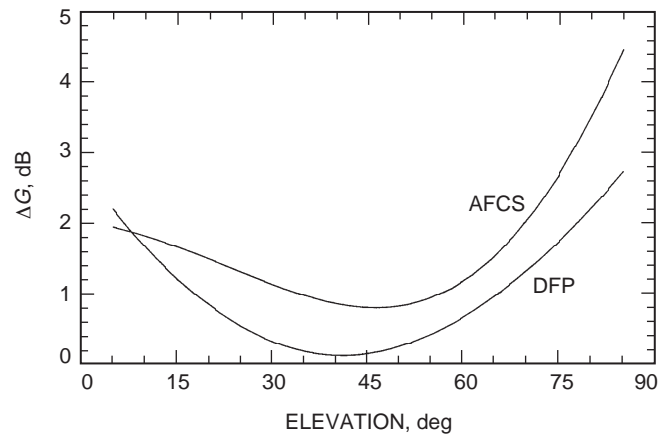

**Fig. 30. Comparison of the gain performance provided
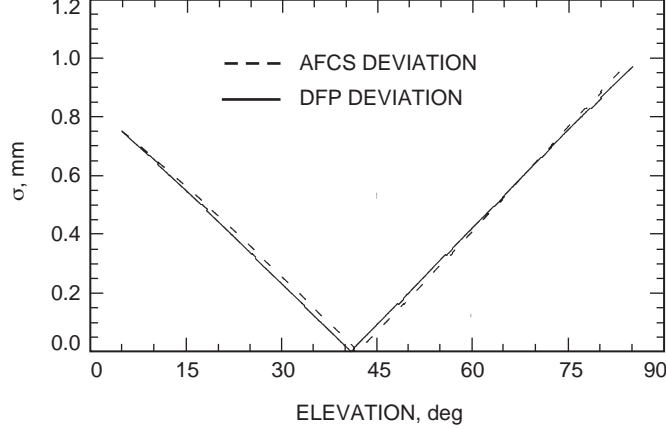by the AFCS and DFP.**

Fig. 31. Comparison of the current baseline rms half-path-length deviations for the AFCS and DFP.

correct DFP shape to achieve compensation for gravity-induced main-reflector deformation at a given elevation angle, it is first necessary to know what the main-reflector deformation is as a function of elevation.

This was determined by first making a series of three sets of measurements at elevations of 12.7, 37, and 47 deg, these being dictated by the availability of suitable 12-GHz (Ku-band) satellite beacons. From the three surface-error maps produced from these measurements, a set of 17 maps was produced at 5-deg intervals, from 5 to 85 deg, by interpolation and extrapolation, and these were used to compute the corresponding phase conjugate DFP shapes and subsequently the DFP actuator displacements required to achieve these shapes.

These maps also serve the purpose of making comparisons between the RF-efficiency measurements and the direct assessment of the main-reflector distortion via holography. Thus, for example, we find that the surface-error map at 40 deg, which is very close to the baseline rigging angles of 42.1 and 40.9 deg determined from the AFCS and DFP efficiency measurements, predicts an rms half-path-length deviation of $\Sigma_0 = 0.73$ mm (see Fig. 32).[20]

On the other hand, Table 3 shows a design control table estimating the Ka-band losses at F1 for the 70-m antenna. Selecting only those terms contributing to amplitude truncation or attenuation, i.e., eliminating the rms and pointing-loss terms, we find the resulting efficiency to be $\varepsilon_a = 0.8191$, and combining this with the above found value for Σ_0, we find

$$\varepsilon_m = \varepsilon_a \exp\left[-\left(\frac{4\pi\Sigma_0}{\lambda}\right)^2\right] = 0.314$$

in excellent agreement with the AFCS and DFP baseline values of 30.7 and 31.2 percent, respectively.[21]

---

[20] The figure of 0.70 mm shown in the map legend represents the computed rms error normal to the reflector surface. The quoted value of 0.73 mm results from transforming this to an axial error and deconvolution to remove the effect of the finite resolution (0.674 m) obtained with the 127-by-127 array size.

[21] We eliminate the pointing error here because great care was taken in the efficiency measurements to ensure that only those data with negligible pointing loss were included in the analysis.
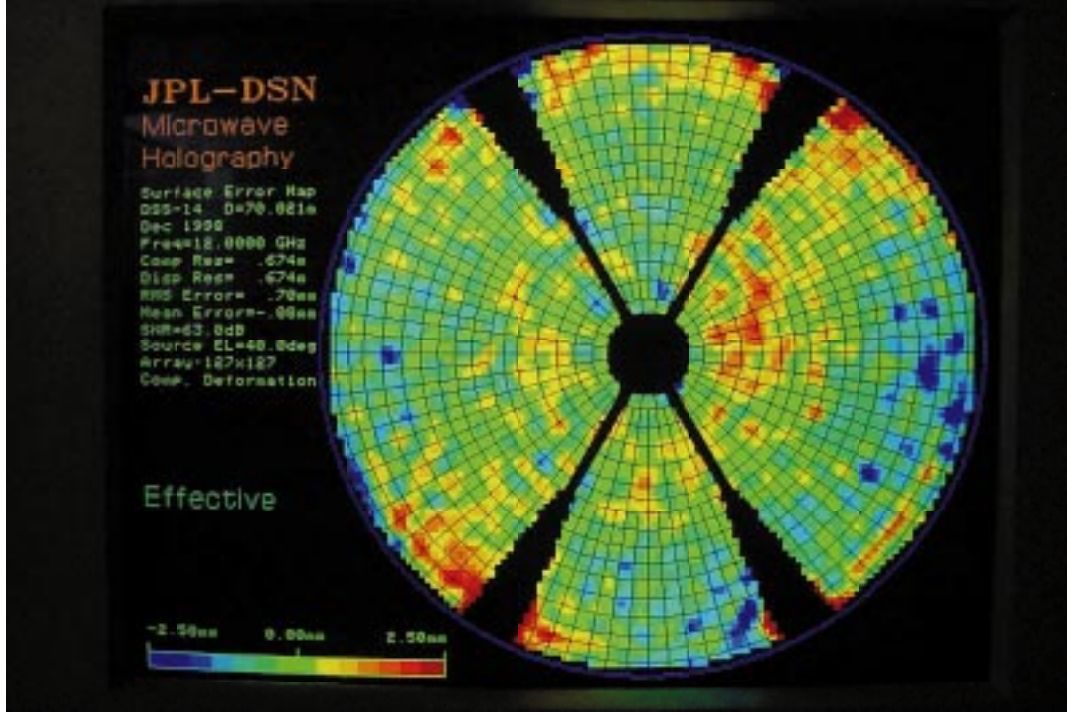
Fig. 32. Effective surface-error map of DSS 14 at 40-deg elevation, derived in December 1998. The rms half-path-length deviation inferred from this is 0.73 mm.

Table 3. Estimated loss factors for the 70-m antenna at DSS 14 at Ka-band.

Item	Ka-band
Main reflector I^{2}R	0.9991
Panel leak	0.9975
Panel gap	0.9982
Surface rms	0.4668
Subreflector I^{2}R	0.9991
Subreflector rms	0.8223
Quadrupod legs	0.9008
Pointing loss	0.9688
Beam squint	0.9954
Subreflector focus	1.0000
Cassegrain VSWR loss	0.9990
Illumination factors	0.9200

Similarly, the map shown in Fig. 33 indicates an rms half-path-length deviation of 0.96 mm at 12.7-deg elevation. This results from a combination of elevation-independent and elevation-dependent contributions, i.e., $\sqrt{\Sigma_0^2 + \Sigma\left(el\right)^2} = 0.96$ mm, so that the elevation-dependent term at 12.7 deg is

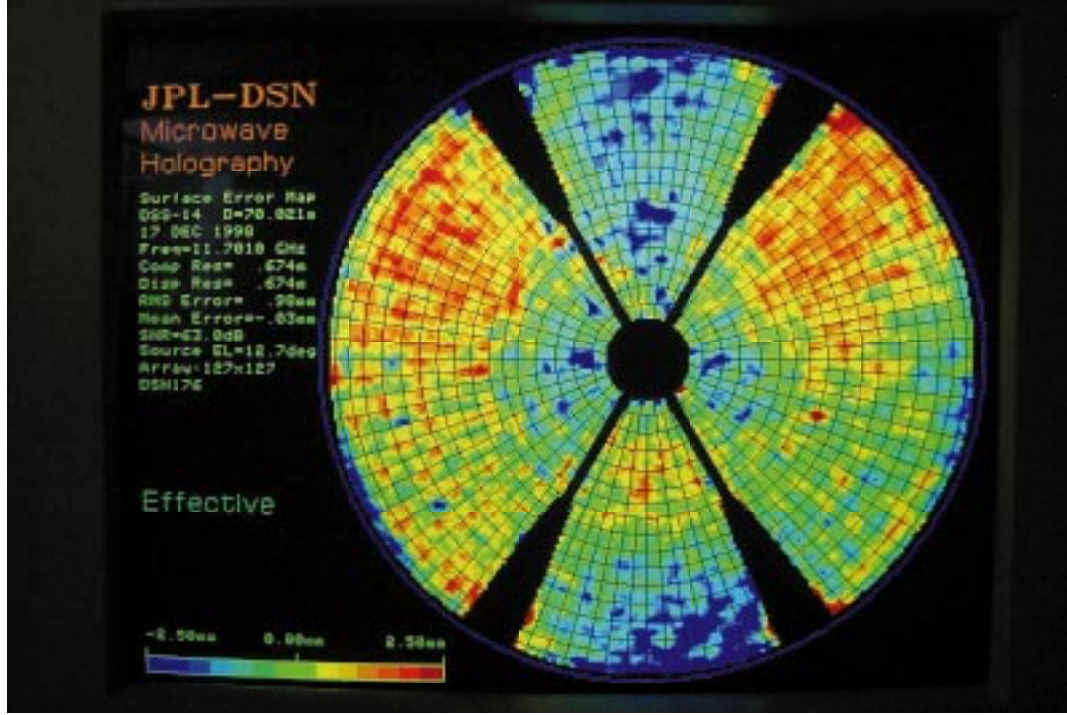$$\Sigma\left(12.7 \text{ deg}\right) = 0.63 \ \text{ mm}$$

Fig. 33. Effective surface-error map of DSS 14 at 12.7-deg elevation, derived in December 1998. The rms half-path-length deviation inferred from this is 0.96 mm, corresponding to a 0.73-mm elevation-independent and a 0.63-mm elevation-dependent contribution.

The corresponding values determined from the AFCS and DFP Ruze–Levy fits are 0.61 and 0.59 mm, respectively (see Fig. 31), again in good agreement.

As a final comparison, in Fig. 34 we show the early DSS-14 Ka-band aperture-efficiency results of Gatti et al. [9] together with the present baseline results. The published efficiency curve for the Gatti results has been slightly modified to reflect the newer values for S_0 and C_{r_0} for VirgoA. The published curve was based on the use of both the planet Venus and VirgoA as calibrators. However, it was discovered that these two radio sources gave considerably different peak-efficiency values, that for Venus being 38 percent and that for VirgoA being 32 percent, and as a result the published curve was based on the Venus data multiplied by 0.92 and the VirgoA data multiplied by 1.08, i.e., a simple average of the two results obtained with the two sources.

The value of 32 percent obtained using VirgoA was based on early estimates of C_{r_0} (1.57) and S_0 (14.68 Jy) for this source, and, when the newer values are used, it is found that the VirgoA data give a peak efficiency of 35.05 percent. Since the value the authors reported is 1.08×32 percent = 34.56 percent, we have multiplied the published efficiency-curve values by the ratio 35.05/34.56=1.0142 to obtain a result that is consistent with the more recent estimates of S_0 and C_{r_0} for VirgoA and with the other two efficiency measurements being considered.

The peak efficiency of the Gatti results is thus approximately 0.53-dB higher than the current baseline results. However, a comparison of the holography results for DSS 14 obtained in 1989, at the time the Gatti measurements were made, with those obtained in 1998 shows an increase in the elevation-independent term, Σ_0, from 0.65 to 0.73 mm, corresponding to a loss of 0.86 dB. The most likely explanation for this difference is the presence of an x- or y-axis subreflector misalignment during the earlier measurements.
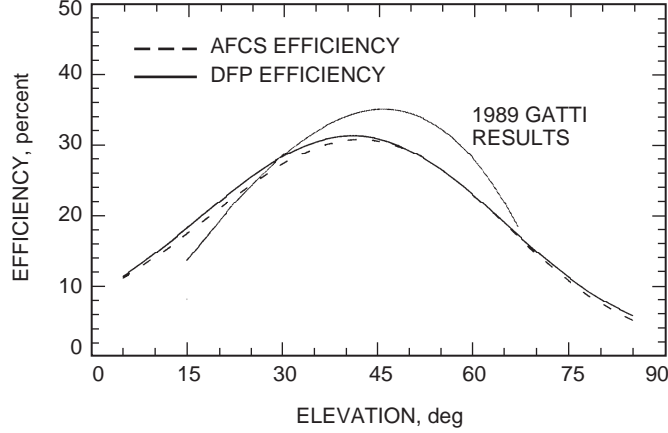
Fig. 34. Comparison of the current baseline efficiency measurements with the earlier Ka-band measurements of Gatti et al.

Also, the measured surface error of the subreflector that resulted from the Landers earthquake is 0.33 mm, and when this is removed from the present total rms surface error of 0.73 mm, one obtains 0.65 mm, in agreement with the original 1989 measurements. It thus appears that the differences between the earlier measurements and the present ones can be accounted for on the basis of the earthquake damage sustained plus a possible misalignment of the subreflector in the x- or y-axis during the early measurements.

VIII. Conclusions

It is shown in this article that the present aperture-efficiency performance of the DSS-14 antenna is marginal at Ka-band as a result of two independent effects, the loss at the rigging angle due to the rms surface error of the main reflector and the loss due to gravity-induced deformation.

Two technologies for compensating for this gravity-induced deformation, the AFCS and the DFP systems, were successfully tested and analyzed at DSS 14.

This article describes in detail the aperture-efficiency performance of the DSS-14 antenna at Ka-band in its present configuration and when used in conjunction with the AFCS and DFP systems, each acting alone. The analysis of the performance is based on data acquired by tracking radio sources at Ka-band. A companion article describes, among other things, the aperture efficiency of the antenna with the AFCS and the DFP systems operating jointly [1]. These results are based on data acquired by tracking the Deep Space One (DS1) spacecraft at Ka-band.

The uncompensated Ka-band aperture efficiency at the mean rigging angle of 41.5 deg is 31.0 ± 1.5 percent, while the gain improvement resulting from the two systems, each acting alone, ranges from approximately 2 dB at low elevations to between 2.7 and 4.4 dB at 85 deg, the higher value corresponding to the AFCS measurements.

In addition, substantial recovery of the antenna-gain loss due to gravity distortion was obtained with the DFP and AFCS systems acting jointly [1]. For example, at the low elevation angle of 8.5 deg, 2.9 dB out of 3.6-dB loss was successfully recovered.

It is shown in Table 3 that the main factor contributing to the antenna-efficiency loss at the rigging angle of 41.5 deg is the main reflector rms surface error of 0.73 mm. Based on previous results and analysis,

it is expected that this figure can be reduced to 0.35 to 0.45 mm, increasing the overall antenna-aperture efficiency to 55 to 60 percent at the rigging angle [10].

Thus, with appropriate panel setting and providing gravity compensation with both systems, the DSS-14 antenna can achieve excellent performance at Ka-band.

Acknowledgments

References

[1] V. Vilnrotter and D. Fort, "Demonstration and Evaluation of the Ka-Band Array Feed Compensation System on the 70-Meter Antennas," *The Telecommunications and Mission Operations Progress Report 42-139, July–September 1999*, Jet Propulsion Laboratory, Pasadena, California, pp. 1–17, November 15, 1999. http://tmo.jpl.nasa.gov/tmo/progress_report/42-139/139J.pdf

[2] T. Y. Otoshi, S. R. Stewart, and M. M. Franco, "A Portable Ka-band Front-End Test Package for Beam-Waveguide Antenna Performance Evaluation—Part 1: Design and Ground Tests," *The Telecommunications and Data Acquisition Progress Report 42-106, April–June 1991*, Jet Propulsion Laboratory, Pasadena, California, pp. 249–265, August 15, 1991. http://tmo.jpl.nasa.gov/tmo/progress_report/42-106/106S.PDF

[3] L. S. Alvarez, "Analysis and Applications of a General Boresight Algorithm for the DSS-13 Beam Waveguide Antenna," *The Telecommunications and Data Acquisition Progress Report 42-111, July–September 1992*, Jet Propulsion Laboratory, Pasadena, California, pp. 48–61, November 15, 1992. http://tmo.jpl.nasa.gov/tmo/progress_report/42-111/111E.PDF

[4] P. H. Richter, "Estimating Errors in Least-Squares Fitting," *The Telecommunications and Data Acquisition Progress Report 42-122, April–June 1995*, Jet Propulsion Laboratory, Pasadena, California, pp. 107–137, August 15, 1995. http://tmo.jpl.nasa.gov/tmo/progress_report/42-122/122E.pdf

[5] C. T. Stelzried and M. J. Klein, "Precision DSN Radiometer Systems: Impact on Microwave Calibrations," *Proc. IEEE*, vol. 82, no. 5, May, 1994.

[6] R. Levy, *Structural Engineering of Microwave Antennas*, IEEE Press, 1996.

[7] P. H. Richter and S. D. Slobin, "DSN 70-Meter Antenna X- and S-Band Calibration Part 1: Gain Measurements," *The Telecommunications and Data Acquisition Progress Report 42-97, January–March 1989*, Jet Propulsion Laboratory, Pasadena, California, pp. 314–351, May 15, 1989.
http://tmo.jpl.nasa.gov/tmo/progress_report/42-97/97GG.PDF

[8] D. J. Rochblatt, "A Microwave Holography Methodology for Diagnostic and Performance Improvement for Large Reflector Antennas," *The Telecommunications and Data Acquisition Progress Report 42-108, October–December 1991*, Jet Propulsion Laboratory, Pasadena, California, pp. 235–252, February 15, 1992.
http://tmo.jpl.nasa.gov/tmo/progress_report/42-108/108R.PDF

[9] M. S. Gatti, M. J. Klein, and T. B. H. Kuiper, "32-GHz Performance of the DSS-14 70-Meter Antenna: 1989 Configuration," *The Telecommunications and Data Acquisition Progress Report 42-99, July–September 1989*, Jet Propulsion Laboratory, Pasadena, California, pp. 206–219, November 15, 1989.
http://tmo.jpl.nasa.gov/tmo/progress_report/42-99/99R.PDF

[10] D. J. Rochblatt, P. M. Withington, and H. J. Jackson, "DSS-24 Microwave Holography Measurements," *The Telecommunications and Data Acquisition Progress Report 42-121, January–March 1995*, Jet Propulsion Laboratory, Pasadena, California, pp. 252–270, May 15, 1995.
http://tmo.jpl.nasa.gov/tmo/progress_report/42-121/121A.pdf